

Revisiting the Chemical Stability of Germanium Selenide (GeSe) and the Origin of its Photocatalytic Efficiency

Danil W. Boukhvalov, Silvia Nappini, Mykhailo Vorokhta, Tevfik Onur Menteş, Lesia Piliai, Mohammad Panahi, Francesca Genuzio, Jessica De Santis, Chia-Nung Kuo, Chin Shan Lue, Valentina Paolucci, Andrea Locatelli, Federica Bondino, and Antonio Politano*

Recently, germanium selenide (GeSe) has emerged as a promising van der Waals semiconductor for photovoltaics, solar light harvesting, and water photoelectrolysis cells. Contrary to previous reports claiming perfect ambient stability based on experiments with techniques without surface sensitivity, here, by means of surface-science investigations and density functional theory, it is demonstrated that actually both: i) the surface of bulk crystals; and ii) atomically thin flakes of GeSe are prone to oxidation, with the formation of self-assembled germanium-oxide skin with sub-nanometric thickness. Surface oxidation leads to the decrease of the bandgap of stoichiometric GeSe and GeSe_{1-x} , while bandgap energy increases upon surface oxidation of Ge_{1-x}Se . Remarkably, the formation of a surface oxide skin on GeSe crystals plays a key role in the physicochemical mechanisms ruling photoelectrocatalysis: the underlying van der Waals semiconductor provides electron–hole pairs, while the germanium-oxide skin formed upon oxidation affords the active sites for catalytic reactions. The self-assembled germanium-oxide/germanium-selenide heterostructure with different bandgaps enables the activation of photocatalytic processes by absorption of light of different wavelengths, with inherently superior activity. Finally, it is discovered that, depending on the specific solvent-GeSe interaction, the liquid phase exfoliation of bulk crystals can induce the formation of Se nanowires.

1. Introduction


Despite the giant impact of the advent of graphene on science^[1] and technology,^[2] the absence of a band gap^[3] has stimulated significant research efforts on van der Waals (vdW) semiconductors,^[4] which afford technological abilities complementary to those of graphene, in various fields, such as photovoltaics,^[5] sensors,^[6] optoelectronics,^[7] and photocatalysis.^[8]

Among the various vdW semiconductors, germanium selenide (GeSe) deserves particular attention,^[9] owing to recent papers reporting its outstanding efficiency for photovoltaics,^[10] solar light harvesting,^[11] and water photoelectrolysis cells.^[12] Specifically, GeSe-based photocathodes displayed a photocurrent density at 0 V versus reversible hydrogen electrode (RHE) of approximately $-11 \mu\text{A cm}^{-2}$ in 0.5 M H_2SO_4 , while GeSe-based photoanodes showed a photocurrent density at +1.2 V versus RHE of $31.0 \mu\text{A cm}^{-2}$ in 1 M KCl.^[12] Furthermore,

D. W. Boukhvalov
College of Science
Institute of Materials Physics and Chemistry
Nanjing Forestry University
Nanjing 210037, P. R. China

D. W. Boukhvalov
Institute of Physics and Technology
Ural Federal University
Mira Street 19, Ekaterinburg 620002, Russia

S. Nappini, F. Bondino
Consiglio Nazionale delle Ricerche (CNR)-Istituto Officina dei Materiali (IOM)
Laboratorio TASC in Area Science Park S.S. 14 km 163.5
Trieste 34149, Italy

 The ORCID identification number(s) for the author(s) of this article can be found under <https://doi.org/10.1002/adfm.202106228>.

© 2021 The Authors. Advanced Functional Materials published by Wiley-VCH GmbH. This is an open access article under the terms of the Creative Commons Attribution-NonCommercial License, which permits use, distribution and reproduction in any medium, provided the original work is properly cited and is not used for commercial purposes.

DOI: 10.1002/adfm.202106228

M. Vorokhta, L. Piliai
Charles University
V Holesovickách 2, Prague 8, Prague 18000, Czech Republic

T. O. Menteş, M. Panahi, F. Genuzio, A. Locatelli
Elettra-Sincrotrone S.C.p.A
S.S. 14-km 163.5 in AREA Science Park
Trieste 34149, Italy

J. De Santis, V. Paolucci
Department of Industrial and Information Engineering and Economics
Via G. Gronchi 18, 7 University of L'Aquila, L'Aquila I-67100, Italy

C.-N. Kuo, C. S. Lue
Department of Physics
National Cheng Kung University
1 Ta-Hsueh Road, Tainan 70101, Taiwan

A. Politano
INSTM and Department of Physical and Chemical Sciences
University of L'Aquila
via Vetoio, L'Aquila, AQ 67100, Italy
E-mail: antonio.politano@univaq.it

A. Politano
CNR-IMM Istituto per la Microelettronica e Microsistemi
VIII strada 5, Catania I-95121, Italy

recent theoretical results indicate that the differential Gibbs free energy for the first step of hydrogen evolution reaction (HER) at Se vacancy defects of GeSe is only 0.073 eV.^[13]

All existing experimental reports also highlight superb chemical stability in GeSe, thus pointing it as an air-stable isostructural and isoelectronic analogue of phosphorene,^[11,12] which instead is affected by rapid degradation in P₂O₅ in ambient atmosphere.^[14] Such conclusions for GeSe were based on the absence of oxide-derived peaks in Raman spectroscopy and X-ray diffraction (XRD).^[11,12] Theoretical models pointed out that the oxidation resistance of monolayer GeSe is significantly higher than that of phosphorene and arsenene, with activation energies for O₂ chemisorption as high as 1.44 eV.^[15] The superior oxidation resistance of GeSe has been recently ascribed to a perovskite-like antibonding valence-band maximum arising from (Ge 4s) – (Se 4p) coupling,^[10] which enables the direct use of unencapsulated devices, without experiencing any efficiency loss even after 1 year in air. Based on such a supposed oxidation resistance, correspondingly, theoretical models explain the photocatalytic activity of GeSe in terms of small exciton binding energy (0.5 eV), particularly suitable for separating photo-generated carriers (holes and electrons).^[16]

Here, we show that this picture should be radically revisited, due to the unambiguous detection of a sub-nanometric surface oxide skin in GeSe, which plays a key role in the physicochemical mechanisms ruling catalytic reactions. Specifically, by means of surface-science tools and density functional theory, we demonstrate the existence of surface oxide phases, whose emergence was overlooked by all previous investigations, due to the insufficient surface sensitivity of spectroscopic and microscopic tools employed so far. Explicitly, Raman spectroscopy has a probing depth in the 300–650 nm range,^[17] largely insufficient to detect a sub-nanometric oxide skin. Moreover, an amorphous oxide layer indeed has no diffraction pattern, in contrast with misleading conclusions on chemical inertness based on XRD in Ref. [12].

Another relevant issue is related to the impact of vacancy defects^[18] on chemical reactivity and ambient stability. Actually, most single crystals of GeSe are far from being stoichiometric. As an example, the [Ge]:[Se] ratio of 45:55 in Ref. [12] implies the occurrence of a significant presence of Ge-vacancy sites, which might—at least supposedly—play a key role in

electrocatalytic and photocatalytic devices,^[12] whose efficiency was instead ascribed to the exfoliation in atomically thin layers. On the other hand, the presence of Se vacancies drastically improves thermoelectric figure of merit zT from 0.2 to 1.35 (at 627 K), owing to metavalent bonding being unfeasible in pristine GeSe.^[19] We demonstrate that the surface transformation of GeSe in germanium-oxide species in ambient conditions is favored by vacancy defects. Precisely, we show that as-exfoliated stoichiometric GeSe single crystal assumes a germanium-oxide skin once it is exposed to air, with a thickness that increases up to 1.5 ± 0.2 nm after prolonged storage (40 days) in ambient atmosphere. The presence of Se vacancies in bulk crystals, as well as the exfoliation in nanosheets naturally exhibiting Se- and Ge-edge sites, accelerates the oxidation process by $\approx 10^5$ times. Furthermore, we shed light on the physicochemical mechanisms ruling the photocatalytic activity of GeSe.

2. Results and Discussion

At room temperature, GeSe crystallizes in an orthorhombic structure (similar to black phosphorus) with space group Pnma, with a Se–Ge–Ge–Se stacking (Figure 1a,b). The high crystalline quality of our grown single crystals is secured by the analysis of both the XRD pattern with preferential [h 0 0] direction (Figure S1, Supporting Information) and the Laue diffraction spots (Figure S2, Supporting Information). The obtained lattice parameters are $a = 10.833$ Å, $b = 3.831$ Å, and $c = 4.394$ Å, in good agreement with previous reports.^[20]

To evaluate the impact of vacancy defects on physicochemical properties, we estimated the formation energies of Se and Ge vacancies in the outermost surface layer of the GeSe bulk crystal, namely the GeSe(100) surface, and in monolayer GeSe. For Se vacancies, we find +2.48 eV/Se for the GeSe(100) surface and +2.14 eV/Se for monolayer GeSe. Similarly, Ge-vacancy defects have a formation energy of +2.47 eV/Ge and +2.16 eV/Ge for GeSe(100) surface and for monolayer GeSe, respectively. Accordingly, we should consider in our theoretical model both types of defects. Definitely, the prevalence of one type of defect over another is defined not by energetics of formation, but rather by synthesis methods. Notably, in spite of their similar formation energies, the impact of Se and Ge vacancies on the

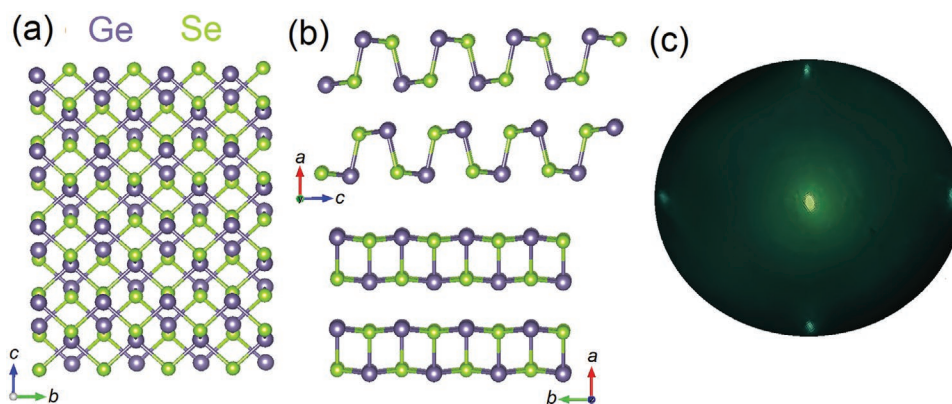


Figure 1. a) Top and b) side view of GeSe atomic structure. Gray and green balls denote Ge and Se atoms, respectively. c) μ -LEED pattern acquired with primary electron beam energy of 14 eV, using a LEEM apparatus. The central spot represents the (00) diffraction.

Table 1. Differential enthalpies and Gibbs free energies of physisorption from gaseous phase and differential enthalpies of further decomposition (all in kilojoules per mole) of molecular oxygen, water, and carbon monoxide on the pristine and defective (100)-oriented GeSe surface and for monolayer GeSe-based systems. The values in parenthesis correspond to the oxidation of whole surface (as depicted in Figure S4, Supporting Information).

Substrate	Adsorbate	ΔH_{ads} [kJ mol ⁻¹]	ΔG_{ads} [kJ mol ⁻¹]	ΔH_{dec} [kJ mol ⁻¹]	
(100)-Oriented surface, bulk crystal	GeSe	O ₂	-18.45	-6.95	-112.79 (-92.06)
		H ₂ O	+23.61	+55.31	+119.83
		CO	+2.18	+21.53	— -171.22
	GeSe _{0.88}	O ₂	-308.30	-296.80	(-102.18)
		H ₂ O	-28.37	+3.33	+10.21
		CO	-56.99	-37.64	— -27.41 (-166.49)
	Ge _{0.88} Se	O ₂	-93.95	-82.45	
		H ₂ O	+19.26	+50.96	+142.62
		CO	-4.00	+15.35	— -1.88 (-446.73)
Monolayer	GeSe	O ₂	+152.98	+164.48	
		H ₂ O	+151.35	+183.05	+154.97
		CO	+154.21	+173.56	— -112.39
	GeSe _{0.88}	O ₂	-98.77	-87.27	(-476.10)
		H ₂ O	+176.64	+208.34	-23.05
		CO	+124.81	+144.16	— -201.78
	Ge _{0.88} Se	O ₂	-269.00	-257.5	(-457.77)
		H ₂ O	-84.35	-52.65	-79.20
		CO	-124.37	-109.02	—

electronic structure of GeSe is different. Specifically, the formation of Se vacancies reduces the value of the bandgap in both bulk (Figure S3a, Supporting Information) and monolayer (Figure S3b, Supporting Information) GeSe. On the other hand, the presence of Ge vacancies transforms the semiconductive bulk GeSe into a semimetal (Figure S3a, Supporting Information). Notably, monolayer Ge_{0.88}Se is even metallic (Figure S3b, Supporting Information).

To assess the chemical stability of GeSe, we computed the differential enthalpy and Gibbs free energy of physisorption of molecular oxygen, water, and carbon monoxide on defect-free and defective surfaces of bulk and monolayer GeSe. Results of the calculations (Table 1) demonstrate that physisorption of molecular oxygen at room temperature is energetically favorable on bulk pristine GeSe (-6.95 kJ mol⁻¹) and, similarly, on defective GeSe (-296.80 kJ mol⁻¹ for GeSe_{0.88} and -82.45 kJ mol⁻¹ for Ge_{0.88}Se, respectively). However, oxygen molecules decompose at room temperature. As a matter of fact, decomposition energy ΔH_{dec} for O₂ is -112.79, -171.22, and -27.41 kJ mol⁻¹ for bulk crystals of GeSe, GeSe_{0.88}, and Ge_{0.88}Se, respectively. The oxygenated surface evolves in all cases into complete surface oxidation (-92.06, -102.18, and -166.49 kJ mol⁻¹ for bulk GeSe, GeSe_{0.88}, and Ge_{0.88}Se, respectively). Thus, oxidation is

exothermic on all GeSe-based systems. Accordingly, based on the theoretical model, we can affirm that oxidation of the surface of pristine GeSe and defective GeSe is unavoidable, contrary to the conclusions of previous reports.^[10–12,15]

Oxygen chemisorption is energetically favorable also for defective monolayers of GeSe, which are particularly prone to complete oxidation (-476.10 and -457.77 kJ mol⁻¹ for GeSe_{0.88} and Ge_{0.88}Se, respectively). Increasing the amount of Se defects in the surface layer up to 33% (GeSe_{0.67}) does not change the formation energy for oxidation significantly (-489.62 kJ mol⁻¹). It is worth noticing that the magnitudes of the differential enthalpies of oxidation of defective monolayers are higher compared to the case of bulk GeSe (both pristine and defective). Thus, the oxidation of GeSe nanosheets is a quick and irreversible process, contrary to conclusions in Ref. [10–12,15].

Remarkably for defect-free monolayer GeSe, physisorption of molecular oxygen results in a significant (up to 10%) change in the lattice constant. The energy cost of these distortions overcomes the energy gain from the physisorption of molecular oxygen, corresponding to positive values of the enthalpy of adsorption (+164.48 kJ mol⁻¹). However, considering the presence of highly reactive edge sites in GeSe nanosheets, we

Table 2. Formation energies for the full surface oxidation and for the decomposition of GeSe into some oxide phases in oxidative environments. Note that the values for the total oxidation of GeSe in Table 1 are reported per mole of oxygen, while in this table values are reported per mole of GeSe. Moreover, ν_{Se} and ν_{Ge} stand for Se and Ge vacancy sites, respectively.

Reaction	Energy [kJ mol ⁻¹]
$\text{GeSe} + 1/2\text{O}_2 \rightarrow \text{GeSeO}$	-46.03
$\text{GeSe}_{0.88} + 1/2\text{O}_2 \rightarrow \text{GeSe}_{0.88}\text{O}$	-51.09
$\text{Ge}_{0.88}\text{Se} + 1/2\text{O}_2 \rightarrow \text{Ge}_{0.88}\text{SeO}$	-83.25
$\text{GeSe} + \text{O}_2 + \nu_{\text{Se}} \rightarrow \text{GeO}_2$	-558.99
$\text{GeSe} + 2\text{O}_2 \rightarrow \text{GeO}_2 + \text{SeO}_2$	-485.75
$2\text{GeSe} + 3/2\text{O}_2 + 2\nu_{\text{Se}} \rightarrow \text{Ge}_2\text{O}_3$	-92.95
$\text{GeSe} + 1/2\text{O}_2 + \nu_{\text{Se}} \rightarrow \text{GeO}$	-88.14
$2\text{GeSe} + 7/2\text{O}_2 \rightarrow \text{Ge}_2\text{O}_3 + 2\text{SeO}_2$	-75.45
$3\text{GeSe} + \text{O}_2 \rightarrow \text{GeO}_2 + \text{Ge}_2\text{Se}_3$	-18.91
$3\text{GeSe} + \nu_{\text{Ge}} \rightarrow \text{Ge}_2\text{Se}_3$	+2.79
$\text{GeSe} + \text{O}_2 \rightarrow \text{GeO}_2 + \text{Se}$	-334.57
$\text{Ge}_{0.88}\text{Se} + 0.88 \text{O}_2 \rightarrow 0.88 \text{GeO}_2 + \text{Se}$	-296.11
$\text{Ge}_{0.76}\text{Se} + 0.76 \text{O}_2 \rightarrow 0.76 \text{GeO}_2 + \text{Se}$	-255.36

can conclude that only the basal plane in defect-free GeSe terraces is not susceptible to oxidation.

To unveil the oxidation mechanisms of GeSe, we calculated the differential enthalpies of several possible oxidation pathways (Table 2). Note that excess germanium or selenium atoms arise from the migration of Ge or Se atoms to sublayers with further passivation of corresponding vacancies. The magnitudes of the differential enthalpies for the oxidation of bulk GeSe-based systems with the formation of oxide skin is rather moderate (below 200 kJ mol⁻¹, see Table 2). The formation of germanium and selenium dioxides as products of reactions in Table 2 is correlated with the differential enthalpies of significantly larger magnitudes than the formation of oxide layers on the surface of GeSe. The formation of other products (Ge₂O₃, GeO, and Ge₂Se₃) corresponds to the negative differential enthalpies of the same order of magnitudes as the formation of the oxide layer. Note that the spontaneous transformation of GeSe into Ge₂Se₃ is energetically unfavorable (+2.79 kJ mol⁻¹).

In the case of Se-rich samples (Ge_xSe) another scenario is feasible. Instead of the passivation of rare Se-vacancies in sublayers, excess Se will form structures, whose shape depends on the conditions for nucleation. As a matter of fact, the total energy per Se atom in amorphous Se agglomerates and Se nanowires is almost the same. The energetics for the decomposition of Ge_xSe to GeO₂ and Se demonstrates the favorability of this process over formation of Ge₂Se₃, Ge₂O₃, and other structures discussed above (Table 2).

Thus, it is demonstrated that in oxidative environments GeO₂ skin is formed over GeSe, while in the case of Se-rich GeSe samples, additional nanocrystalline Se-based structures could be formed.

In the case of GeSe-based monolayers, oxygen decomposition is also an exothermic process with higher magnitudes of the differential enthalpy (ranging from up to -476.10 kJ mol⁻¹

for GeSe_{0.88} and up to -446.73 for GeSe). In summary, we can describe the oxidation of the surface of bulk GeSe as a three-step process. The first step consists in the formation of GeSeO surface layer. In the second step, the surface GeSeO layer is transformed into a combination of GeO, Ge₂O₃, and Ge₂Se₃ structures (note that the ratio of these structures is defined by the Ge to Se ratio in surface layers before oxidation). In the third step, these multiple structures are transformed into GeO₂, SeO₂, and Se-nanostructures. Thus, oxidation of monolayer germanium selenide is an irreversible process.

The surface oxide skin could in principle affect the photocatalytic processes. Notably, we find that the transformation of the oxygenated GeSe surface, that is, GeSeO (early steps of the oxidation) into the GeO₂ skin achieved after complete oxidation does not jeopardize the capabilities of bulk GeSe as a light harvester in photocatalytic devices. Actually, surface oxidation in bulk GeSe crystals leads to the decrease of the bandgap of GeSe and GeSe_{0.88}, while bandgap energy slightly increases in Ge_{0.88}Se (Figure S3c, Supporting Information). Note that in the case of Ge-deficient GeSe, surface oxidation induces the quenching of electronic states around the Fermi level, turning Ge_{0.88}Se from metal to semiconductor. Therefore, upon oxidation of the GeSe surface (Figure S4, Supporting Information), a self-assembled GeO₂/GeSe heterostructure with different bandgaps is formed. Therefore, photocatalytic processes are activated by absorption of light of different wavelengths, with inherently higher activity. Specifically, as shown in Figure S3d, Supporting Information, of the bandgap of GeO₂ is significantly larger than that of GeSe (2.78 eV for GeO₂ versus 1.11 eV for GeSe). We also considered the effect of the surface oxidation on the change of the work function. The calculated work function for few layers of GeSe is ≈3.9 eV. The presence of Ge vacancies leads to an increase of the work function up to the value of 4.1 eV, while the presence of Se vacancies induces a decrease of the work function to 3.5 eV. The magnitude of the dipole moment of a GeSe slab changes from -0.01 Dy in defect-free GeSe to -0.25 and -0.18 Dy in the presence of Ge and Se defects, respectively. The formation of the GeSeO surface layer (see Figure S5, Supporting Information) provides an increase of the dipole moment of the slab and of the work function up to the value of -0.58 Dy and 4.6 eV, respectively. The calculated charge transfer from the GeSeO layer to subsurface layers is 0.54 e⁻/GeSe. Remarkably, due to the weak interlayer coupling in GeSe, all transferred charge is localized only on subsurface non-oxidized GeSe layer (see Figure S5, Supporting Information) and the electronic structure of the deeper subsurface area of GeSe is not influenced by the formation of the GeSeO layer on the surface. We also assessed the work function of thin slabs of GeO₂. A value of the work function of ≈4.5 eV corresponds to a GeO₂ slab of 5 nm or a GeO_{2-x} slab of 4 nm. Thus, an increase of the work function upon oxidation can be related to the formation of GeSeO surface layer or the formation of a GeO_{2-x} skin of a few nanometers. Notably, a similar increase of work function by ≈0.3 eV upon air exposure is observed also in our x-ray photoemission measurements.

Additionally, GeO₂ formation corresponds to the healing of the defects in the surface of the bulk crystal, thus decreasing the amount of the possible centers for the recombination of photogenerated electron-hole pairs. Accordingly, our

calculations demonstrate that oxidation of the surface of GeSe leads to improvement of photocatalytic performance.

Concerning the reactivity of the GeSe towards water at room temperature, its physisorption is unfavorable on pristine GeSe, as indicated by the positive value of the differential Gibbs free energy ($\Delta G = +55.31 \text{ kJ mol}^{-1}$). While Ge vacancies do not significantly influence water physisorption ($\Delta G = +50.96 \text{ kJ mol}^{-1}$ in $\text{Ge}_{0.88}\text{Se}$), the existence of Se vacancy sites drastically reduces the differential Gibbs free energy for water physisorption ($\Delta G = +3.33 \text{ kJ mol}^{-1}$ in $\text{GeSe}_{0.88}$). Correspondingly, also water decomposition is energetically unfavorable for all bulk GeSe-based compounds ($+119.83$, $+10.21$, and $+142.62 \text{ kJ mol}^{-1}$ for GeSe, $\text{GeSe}_{0.88}$, and $\text{Ge}_{0.88}\text{Se}$, respectively). Increasing the number of defects in the supercell ($\text{GeSe}_{0.76}$ and $\text{Ge}_{0.76}\text{Se}$) does not make adsorption of water favorable at room temperature. We also assessed the possibility of water intercalation in the sub-surface region of defect-free GeSe. The differential enthalpy of this process is $+108.36 \text{ kJ/H}_2\text{O}$. Therefore, we can rule out the occurrence of water intercalation in humid environments. Thus, taking into account additional energy costs for breaking hydrogen bonds in liquid phase, we can affirm that all GeSe-based systems are undeniably stable in water. Accordingly, we conclude that both GeSe-based bulk systems are unsuitable catalysts for water splitting (oxygen evolution reaction (OER) and HER in alkali media). This result is in good agreement with the stable performance of GeSe photocatalyst in water media.^[12,21]

In the case of defect-free GeSe-monolayers, the general features of the interaction with water are similar to the case of the bulk. The presence of Se vacancies in monolayer GeSe favors water decomposition. On the other hand, the eventual presence of Ge vacancies switches water physisorption and decomposition to exothermic. Thus, taking into account possible delamination of GeSe in liquid water, the stability of GeSe depends on the deviation from stoichiometric conditions and, especially, from the abundance of Ge vacancies.

Concerning the reactivity towards carbon monoxide (relevant in order to assess eventual CO poisoning of the electrode^[22]), results in Table 1 indicates that CO physisorption is favorable at room temperature only on Se vacancies at the surface of defective bulk crystal ($\text{GeSe}_{0.88}$). In the case of prevalence of Ge-vacancy defects ($\text{Ge}_{0.88}\text{Se}$), we can assume bulk GeSe-based systems to be CO-tolerant.

Beyond evaluation of light harvesting and surface chemical reactivity, we also evaluated the electrocatalytic activity of GeSe-based systems. Considering that the adsorption of water from the liquid phase on the GeSe and $\text{GeSe}_{0.88}$ surfaces is unlikely, we excluded OER (water splitting) and HER in alkali media from consideration. Calculated free energies for Volmer–Heyrovsky steps of HER in acidic media ($\text{H}^+ \rightarrow \text{GeSe}_x\text{-H}$, then $\text{GeSe}_x\text{-H} + \text{H}^+ \rightarrow \text{H}_2$) demonstrate rather high energy cost for this process in the case of defect-free bulk and monolayer GeSe ($+1.03 \text{ eV/H}^+$ and $+1.14 \text{ eV/H}^+$, respectively). The oxidation of the surface of GeSe with the formation of a surface GeO_2 skin additionally increases the energy cost of Volmer step up to $+2.63 \text{ eV/H}^+$. On the other hand, the presence of Se (Ge) vacancies corresponds to an energy cost of Volmer step of $+0.25$ ($+0.27$) eV/H^+ and 0.10 (0.08) eV/H^+ for bulk and monolayer defective GeSe-based system (Figure 2). Such obtained values are comparable with state-of-the-art Pt-based electrodes. Note

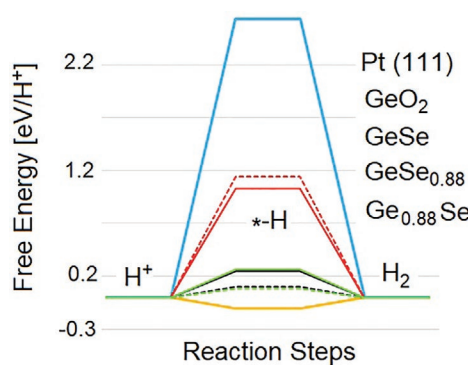


Figure 2. Calculated free energy diagram for HER in acidic media over bulk (solid lines) and monolayers (dashed lines) of GeSe, $\text{GeSe}_{0.88}$, $\text{Ge}_{0.88}\text{Se}$, and GeO_2 . The value for Pt(111) is reported as reference.

that in contrast to GaSe, where only formation of Ga_2O_3 makes bulk system feasible for electrocatalysis,^[23] defective GeSe systems are excellent catalysts. Thus, considering the various advantages afforded by GeSe, that is, its cheapness, water stability, and CO tolerance, we can propose GeSe as a suitable (photo)catalyst in liquid media.

Recent theoretical works^[13,24] predicted rather low barrier ($\approx 0.1 \text{ eV/H}^+$) for HER on defective (100) surface of GeSe. Note that in Refs. [13,24] modelling was performed for monolayers, taking into account only the optimization of atomic positions. However, this approach excludes from consideration either the influence of sublayers in bulk samples or the underlying substrates in few-layer samples. Furthermore, also in the monolayer regime, the flexibility of free-standing membrane should be carefully considered in theoretical models, as it can significantly influence energetics of the adsorption, as recently demonstrated for the case of InSe and GaSe nanosheets.^[23] Other works^[16,25] considered a possible catalytic efficiency of β -GeSe (i.e., an allotrope with distorted h-BN structure). The β -GeSe allotrope can be discussed as a model of (001)-oriented surface of GeSe in ground state tetrahedral phase or grain boundaries.

Our theoretical predictions (Tables 1 and 2) were supported by experimental findings with surface-science techniques (Figures 3–5). Specifically, the surface reactivity of pristine and defective GeSe towards H_2O and O_2 was experimentally investigated by X-ray photoemission spectroscopy (XPS) using complementary experimental apparatuses, which are able to provide a complete overview of the GeSe stability, thus clarifying the role of surface oxide phases formed in the presence of atmospheric gases for both bulk crystals and nanosheets.

The modification of a defect-free GeSe surface, cleaved in ultra-high vacuum (UHV), upon different O_2 and H_2O doses (up to 10^6 L , $1 \text{ L} = 10^{-6} \text{ Torr} \cdot \text{s}$) was investigated by high-energy resolution synchrotron radiation XPS measurements with high surface sensitivity (probing depth $\approx 2.1 \text{ nm}$). As reported in Figure 3, the as-cleaved GeSe sample displays a single doublet in the Ge 3d and Se 3d core levels with a binding energy (BE) of J = 5/2 components at 30.0 and 54.0 eV, respectively, congruently with previous reports.^[26]

Upon exposure to water vapor, new components emerge (Figure 3a,b) and progressively increase with increasing

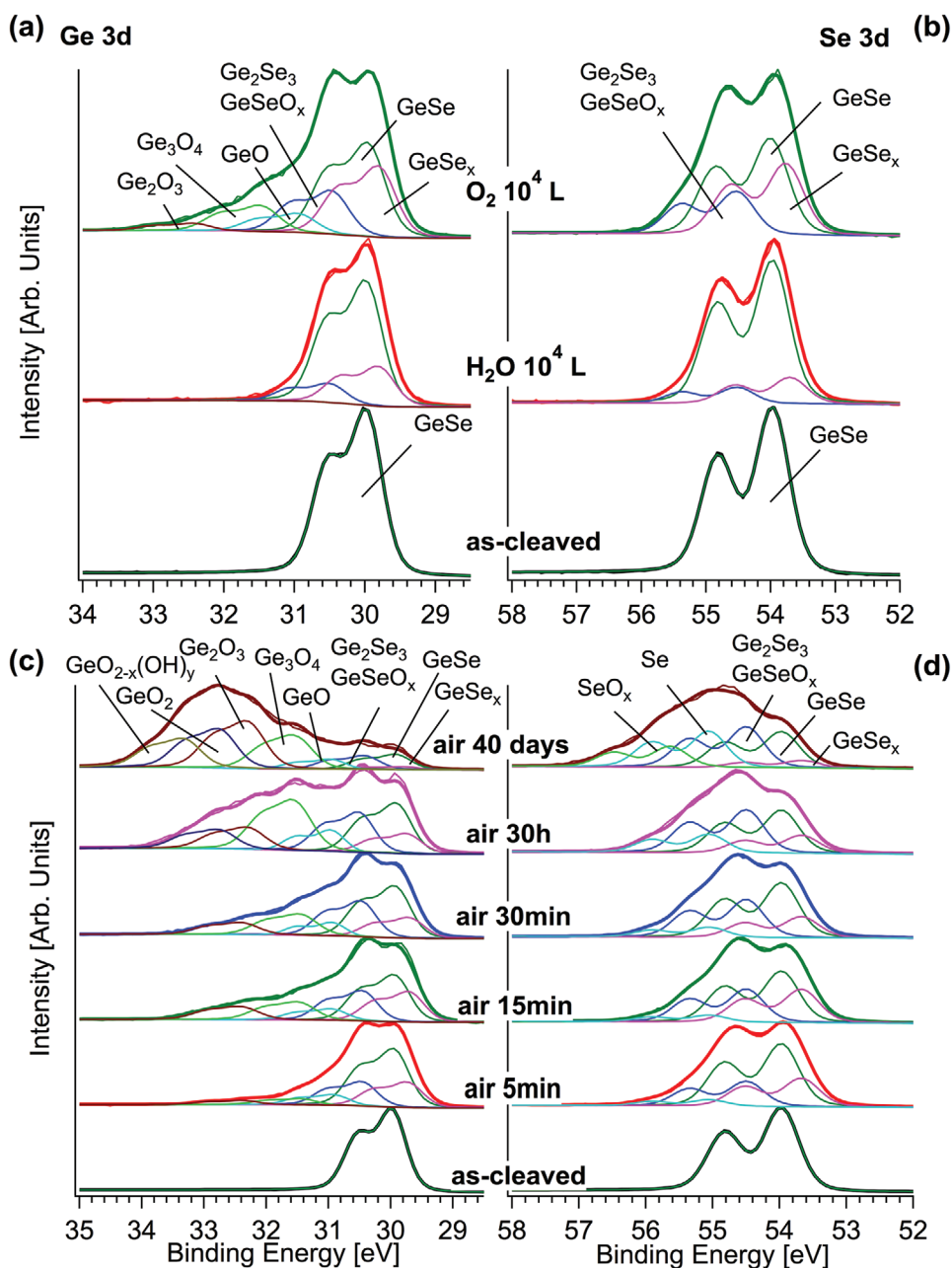


Figure 3. a) Ge 3d and b) Se 3d core levels collected from defect-free GeSe surface and after exposure to 10^4 L of H_2O and O_2 . c) Ge 3d and d) Se 3d core levels collected from the same surface after subsequent exposures to air. The spectra were collected at an emission angle of 60° with a photon energy of 650 eV.

doses (Figure S7a,b, Supporting Information), while keeping similar intensity ratio with respect to each other. A new component ($GeSe_x$) assigned to the formation of a Se-depleted phase appears at 29.8 eV in Ge 3d ($\approx 22\%$ of the total spectrum area) and at 53.7 eV in Se 3d ($\approx 14\%$ of the total spectrum area) (see Figure 3a,b), similarly to $GaSe$.^[23] On the high BE side of the main $GeSe$ peak, components located at 30.6 eV in Ge $3d_{5/2}$ ($\approx 10\%$ of the total spectrum area) and at 54.5 eV in Se $3d_{5/2}$ ($\approx 9\%$ of the total spectrum area) are assigned to the formation of Ge_2Se_3 ^[27] or to early stage oxidized species, such as $GeSeO_x$.

The defect-free GeSe surface was also exposed to 10^4 L of molecular oxygen (Figure 3a,b), evidencing a much higher surface reactivity in comparison to the same dose of water, consistently with theoretical predictions. The Ge 3d core level (Figure 3a) of O_2 -exposed sample shows, besides the $GeSe_x$ ($\approx 27\%$ Ge 3d and $\approx 34\%$ Se3d spectra area) and Ge_2Se_3 - $GeSeO_x$ ($\approx 17\%$ Ge 3d and $\approx 21\%$ Se 3d spectral area) components, additional features located at BEs of 30.9, 31.4, and 32.4 eV, which can be identified with Ge oxides having different oxidation states: GeO (Ge^{2+} , $\approx 7\%$), Ge_3O_4 (Ge^{2+}/Ge^{3+} , $\approx 10\%$), and Ge_2O_3 (Ge^{3+} , $\approx 3\%$), respectively.^[28] The peaks corresponding to a

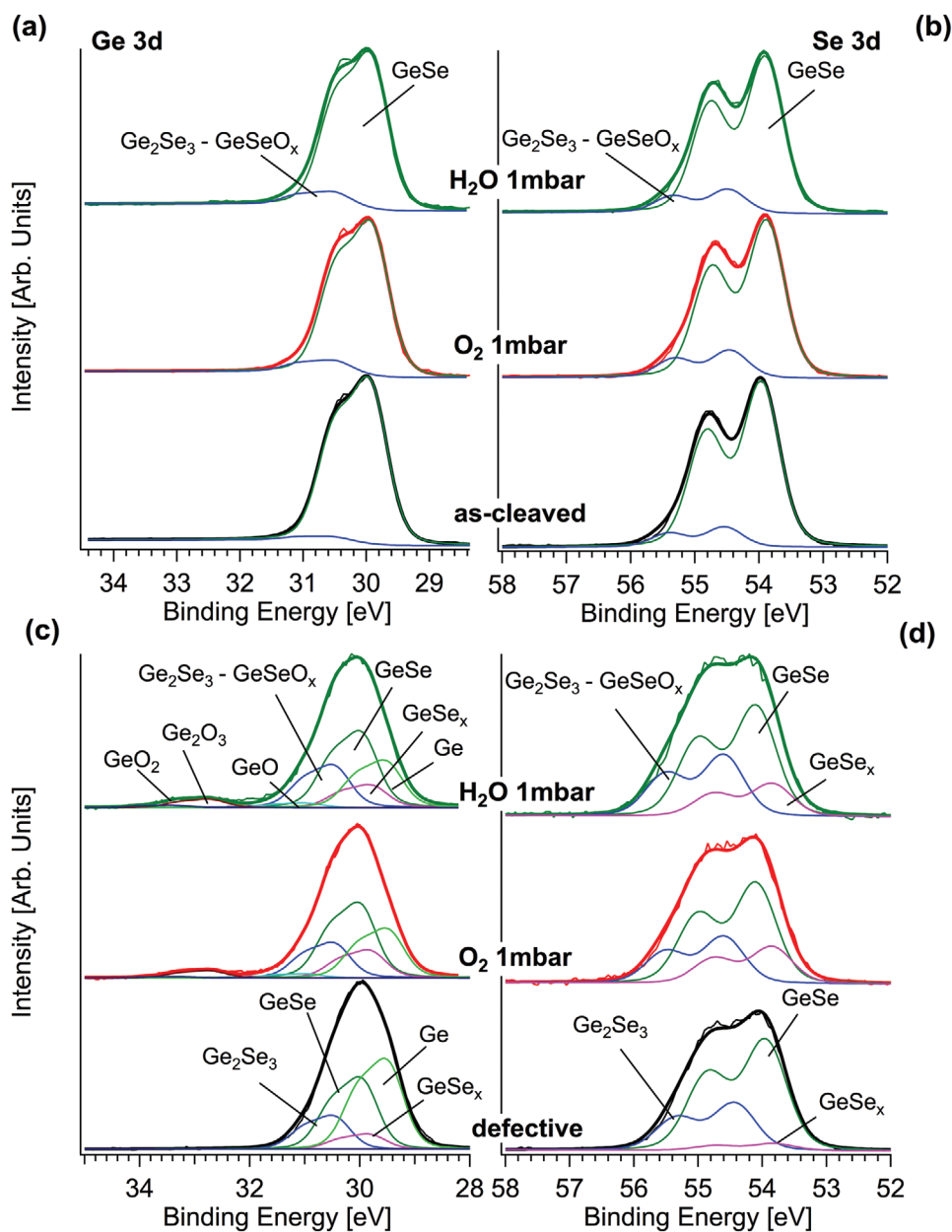


Figure 4. Ge 3d and Se 3d core levels from defect-free GeSe (a,b) and defective GeSe (c,d) surfaces upon exposures to 1 mbar O₂ and a subsequent exposure to 1 mbar H₂O. The spectra were collected at an emission angle of 90° with a photon energy of 1486.6 eV in a NAP setup.

higher oxidation state progressively grow up with increasing O₂ doses (Figure S7c,d, Supporting Information), consuming GeSe. The thickness of the mixed phase of different Ge oxides after a dose of 10⁶ L O₂ was estimated to be ≈(0.4±0.1) nm through quantitative XPS methods, described in Section S4, Supporting Information.

The as-cleaved GeSe surface was then exposed to ambient air in order to investigate aging phenomena (Figure 3c,d). After only 5 min in air, spectral components associated with Ge oxidation are observed, evidencing a strong reactivity of the GeSe surface in atmospheric conditions. From quantitative XPS, it could be estimated that a skin of mixed Ge oxides of ≈(0.3±0.1) nm is present after this short-term exposure to air.

Se 3d also displays a new component at high BE (55.1 eV) associated with the formation of elemental Se,^[29] which was not visible after O₂ and H₂O dosage in UHV conditions. For longer air exposure, the intensity of Ge₂Se₃-GeSeO_x as well as that of intermediate oxide components (GeO, Ge₂O₃, and Ge₃O₄) increases, and after 30 h in air a new feature at 32.7 eV appears (≈9% of the total Ge3d area), which can be ascribed to the formation of GeO₂ (Ge⁴⁺). Finally, after 40 days the intermediate oxides have been partially converted into GeO₂ (≈21%) and a new component due to mixed oxide-hydroxide GeO_{2-x}(OH)_y emerges at 33.3 eV (≈15%).^[30] It is likely that some water molecules are captured and dissociated on GeO₂ surface to form the HO-Ge=O bond, which is expected to have higher

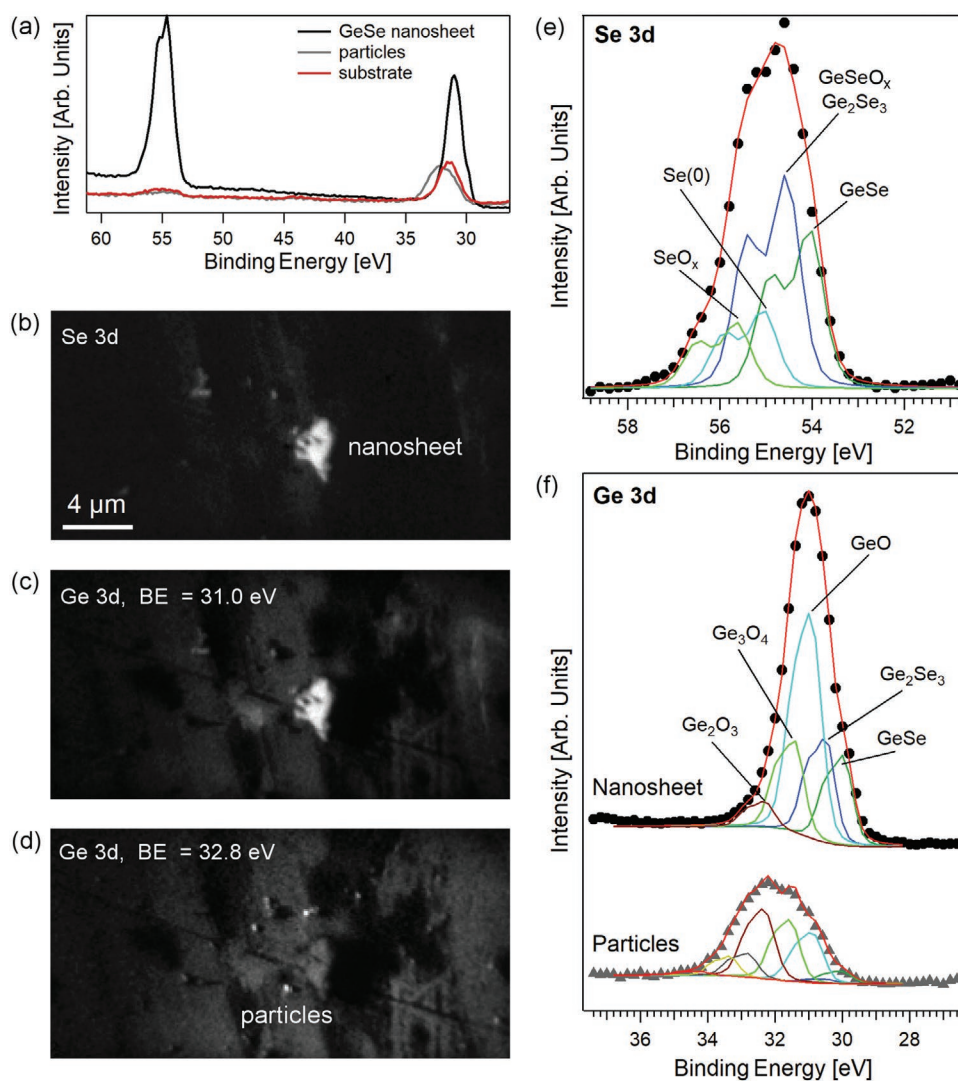


Figure 5. a) μ -XPS spectra of three different selected areas in GeSe nanoflakes drop-casted on a gold-coated silicon substrate. XPEEM images are shown at the b) Se 3d, c) Ge 3d (BE = 31.0 eV), d) Ge 3d (BE = 32.8 eV) core levels. The GeSe nanosheet is visible in the Se 3d XPEEM image displayed in (b), whereas the Ge particles are shown in (d). Se 3d and Ge 3d XPS spectra of GeSe nanoflakes, fitted with the same parameters used for GeSe single crystal, are reported in panels (e) and (f), respectively. The spectra were collected with a photon energy of 150 eV.

BE due to the difference in electronegativity between O and Ge atoms.^[30]

In Se 3d spectra, the component associated with elemental Se progressively increases with air exposure and an additional component grows up at 55.6 eV after 40 days ($\approx 15\%$), which is possibly ascribed to the formation of SeO_x sub-oxide species (Se^{2+} or Se^{3+}).^[31]

A final oxide thickness of $\approx (1.5 \pm 0.2)$ nm after 40 days in air was estimated by quantitative XPS analysis of Ge 3d core level (Section S4, Supporting Information).

Near-ambient pressure X-ray photoemission (NAP-XPS) experiments in controlled atmosphere were carried out to compare the reactivity of both pristine (Figure 4a,b) and defective GeSe (Figure 4c,d) surfaces upon exposure to a partial pressure of 1 mbar of H_2O and 1 mbar of O_2 gases for 1 h, corresponding to a total dose of 10^{10} L. O 1s spectra show the typical spectral features of O_2 (double peaks in the 536–540 eV range)

and H_2O (BE = 535.6 eV) in gas phase (Figure S8, Supporting Information). Despite the higher gas pressure used in the NAP chamber during XPS spectra acquisition, no relevant modification of Ge 3d and Se 3d core levels was observed in the pristine GeSe surface (Figure 4a,b). This can be explained considering that the NAP-XPS apparatus has a lower surface sensitivity (core level probing depth ≈ 8.5 nm) and a lower energy resolution in comparison to the synchrotron radiation measurements as discussed above (Figure 3a,b), thus it is clear that the spectra reported in Figures 3 and 4 cannot be quantitatively compared.

To investigate surface chemical reactivity of a defective GeSe surface, we introduced Se vacancies by sputtering the surface with Ar ions, so as to modify the stoichiometric GeSe sample into a $\text{GeSe}_{0.6}$ surface (in which also a minor component of Ge_2Se_3 is present). The emergence of a component at BE = 29.5 eV in Ge 3d is consistent with the presence of metallic Ge on the

surface,^[28b,32] as expected after the creation of Se vacancies in GeSe_{0.6}. The evolution of core levels in GeSe_{0.6} during the exposure to 1 mbar O₂ in the NAP-XPS apparatus shows that the intensity of GeSe_x components slightly increases (up to ≈20%), metallic Ge decreases, and that new features are ascribed to Ge₂O₃ and GeO₂^[28] (≈4% of Ge 3d spectrum area) emerge (Figure 4c,d). A comparison between pristine and defective GeSe core levels, both measured in the same NAP experimental conditions, clearly confirm that the defective GeSe sample is more prone to oxidation in comparison to the defect-free GeSe surface, in agreement with our theoretical predictions (Table 1).

Beyond single crystal surfaces, we also investigated GeSe nanosheets obtained by liquid-phase exfoliation (see Experimental Section), which are expected to be efficient electrocatalysts, due to the presence of defects and highly reactive edge sites. Atomically thin layers of GeSe are prone to strong oxidation at the edge sites, which are particularly active toward reactions with ambient gases, solvents, and electrolytes employed for exfoliation and electrocatalysis. To prove the inevitable oxidation of exfoliated GeSe nanosheets, we measured Ge-3d (Figure S9a, Supporting Information) and Se-3d (Figure S9b, Supporting Information) core levels of GeSe flakes deposited on an Au-covered Si wafer using synchrotron radiation, which provides an average picture of the nanoflakes composition with a high surface sensitivity. The rather complex spectra obtained from laterally averaging high-resolution XPS measurements indicated the presence of a heterogeneous surface (Figure S9, Supporting Information). Therefore, we carried out spatially resolved X-ray spectromicroscopy measurements (Figure 5) with synchrotron radiation in order to sort out the different features present on the surface. In Figure 5a, the Ge 3d and Se 3d spectra corresponding to GeSe nanosheets, Ge nanoparticles, and elsewhere on the Au/Si substrate were extracted from the regions indicated in the X-ray photoemission electron microscopy (XPEEM) images in Figure 5b–d. The isolated GeSe nanosheets can be easily discerned in the Se 3d XPEEM image in Figure 5b. The dimensions of single flakes range from a few hundred nanometers to several micrometers. In addition to the GeSe, there are sub-micrometer particles predominantly containing elemental Ge. The core-level shifts at the Ge 3d peak between the GeSe flakes and the Ge particles allow us to distinguish them in XPEEM imaging, and thus

the Ge 3d image at higher BE in Figure 5d highlights the Ge particles.

The chemical state of the GeSe nanosheets can be determined from fitting the Se 3d (Figure 5e) and Ge 3d (Figure 5f) peaks bearing in mind BEs obtained for the GeSe single crystal (Figure 3). The component at the lowest BE in each core-level spectrum matches BEs found for the as-cleaved single-crystal sample. However, the predominant spectral weight in μ-XPS spectra of GeSe nanosheets in the region of Ge 3d arises from the oxidized species.

The thickness of the chemically modified part of the surface of the GeSe nanosheets can be estimated from the suppression of the core-level components for stoichiometric GeSe. In order to do this, we make the approximation by using the energy-dependent electron inelastic mean free path in Ge.^[33] Both Se and Ge peaks result in similar values for the surface skin thickness, which is ≈0.68 ± 0.05 nm.

The analysis of the Ge 3d core level for Ge particles indicates that elemental Ge is absent, pointing out that it is much less resistant under an oxidizing environment in comparison to the GeSe flakes. Interestingly, in addition to the more abundant GeSe flakes and GeO_x particles, also very long and straight Se nanowires are found on the surface. One typical nanowire of 4 μm length is displayed in **Figure 6**. The BEs of the two Se 3d_{5/2} components in the nanowire (55.5 and 55.3 eV, respectively) are in excellent agreement with the values reported for amorphous Se nanowires.^[34] Therefore, we conclude that part of the GeSe is decomposed during the exfoliation process to form amorphous Se nanowires along with a nearly uniform background of GeSe nanosheets and Ge particles. We note that the large variations in the surface distribution of each constituent resulting from the drop-casting, along with the small field-of-view of the x-ray microscopy measurement, rule out a reliable determination of the relative abundance of nanosheets compared to the Se nanowires.

For the sake of completeness, we mention that the SeO₂ signal is absent in all Se-3d core-level spectra for both bulk crystals and nanosheets of GeSe, as evident from the lack of spectral contributions at a BE ≈60 eV^[35] (see Figure 6 for nanosheets and Figure S12, Supporting Information, for bulk crystals).

To get more insights regarding Se nanowires produced together with nanosheets in the liquid-phase exfoliation

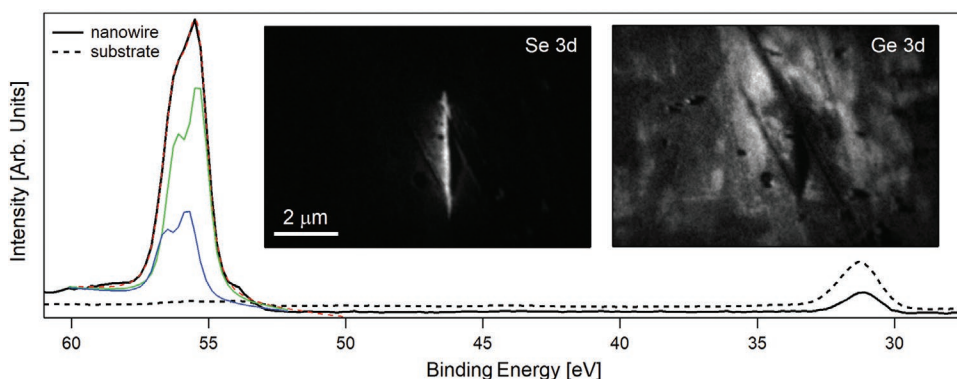


Figure 6. XPS data from a typical Se nanowire (formed in the IPA-assisted liquid-phase exfoliation) are shown along with the XPEEM images at the Se 3d and Ge 3d core levels. Note that the nanowire displays a length of ≈4 μm and it contains only minimal traces of Ge. Photon energy is 150 eV.

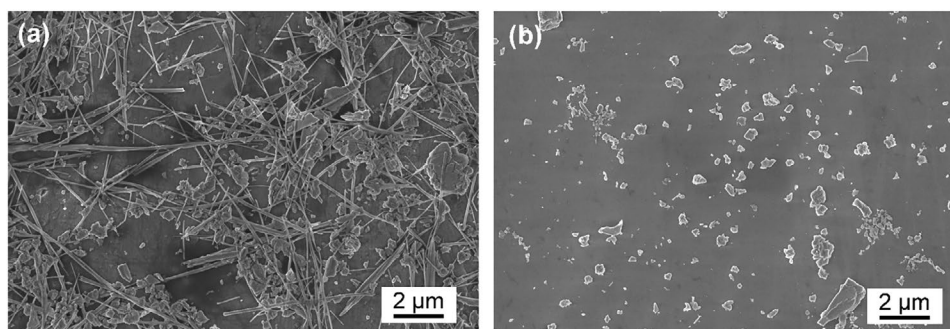


Figure 7. SEM images of GeSe nanosheets exfoliated in liquid phase by using a) IPA (same sample of Figures 5 and 6) and b) dimethyl 2-methylglutarate. The presence of nanowires is evident only in IPA-assisted exfoliated nanosheets of GeSe. See also Figure S10, Supporting Information, for SEM images of nanosheets achieved with liquid-phase exfoliation assisted by ethanol and NMP.

process, we assessed the role of solvents in the formation of Se nanowires through a systematic investigation using different solvents. Precisely, we exfoliated GeSe bulk single crystals in liquid phase using: a) isopropyl alcohol (IPA) (see scanning electron microscopy, SEM, image in **Figure 7a**); b) dimethyl 2-methylglutarate (**Figure 7b**); c) *N*-methyl-2-pyrrolidone (NMP) (**Figure S10a**, Supporting Information); and d) ethanol (**Figure S10b**, Supporting Information). Notably, Se nucleation occurs only when using IPA as solvent. Nucleation of Se nanowires occurs by abstraction of Se from the surface of GeSe nanosheets with further aggregation with wire-like morphology. We can propose that the value of the dielectric constant (17.9 versus 3.8 at room temperature for NMP and IPA, respectively) and of the dipole moment (4.1 D versus 0.76 D for NMP and IPA, respectively) play a crucial role in the ultimate morphology and size of the nanostructures obtained in the liquid-phase exfoliation of bulk crystals, as recently discussed in literature^[36] (see also Ref. [37] for a review).

Finally, to probe the effects of GeSe oxidation on electric properties, we carried out real-time monitoring of the evolution of electrical resistance of GeSe subjected to five consecutive cycles of mild thermal treatment in the 25–100 °C range. The electrical resistance (Figure S11, Supporting Information) progressively increased by more than two orders of magnitude after just two cycles. This behavior is fully consistent with the indication by surface-science techniques (Figures 3–5) and can be explained with the larger bandgap associated with GeO₂ as compared to GeSe (i.e., 2.78 eV and 1.11 eV respectively, as measured in Figure S3, Supporting Information). Accordingly, GeSe oxidation has a dramatic impact for any device application requiring thermal treatments. On the other hand, recently it has been claimed that uncapped GeSe photovoltaic devices show perfect stability even after 60 thermal cycles from –40 to 85 °C,^[10] without any noticeable change in the efficiency.

3. Conclusions

GeSe is commonly assumed as a vdW semiconductor with outstanding chemical stability and superior oxidation resistance even after prolonged storage in air. Here, we have

unveiled the key features of its chemical reactivity and, correspondingly, the real physicochemical mechanisms ruling its photocatalytic activity. Specifically, contrary to previous reports claiming ambient stability of GeSe, by using a combination of surface-science techniques and density functional theory, we have demonstrated that both: i) the surface of bulk crystals; and ii) atomically thin layers of GeSe are susceptible to oxidation, with the formation of germanium-oxide skin with sub-nanometric thickness. Surface oxidation induces the decrease of the bandgap of stoichiometric GeSe and GeSe_{1-x}, while bandgap energy rises in oxidized Ge_{1-x}Se. Notably, the formation of a surface oxide skin on GeSe crystals plays a pivotal role in the physicochemical mechanisms ruling photoelectrocatalysis. As a matter of fact, the underlying vdW semiconductor afforded electron–hole pairs, while the germanium-oxide skin formed upon oxidation provides the active sites for catalytic reactions. The self-assembled germanium-oxide/germanium-selenide heterostructure with different bandgaps enabled the activation of photocatalytic processes by absorption of light of different wavelengths, with intrinsically superior activity.

Concerning electrocatalysis with GeSe, we have demonstrated its water stability and tolerance to CO poisoning, thus we can propose GeSe as prospective (photo)catalyst in liquid media, also considering its cheapness.

Finally, we discover that, in addition to GeSe nanosheets, Se nanowires are formed whenever GeSe is exfoliated with IPA solvent, while liquid-phase exfoliation assisted by other solvents prevent the agglomeration of Se nanostructures.

Our results are crucial to bring to fruition GeSe in technology, with direct implications for any GeSe-based application in the fields of catalysis, energy, nanoelectronics, and nanoscience.

4. Experimental Section

Growth: Generally, GeSe crystals were synthesized using the Bridgman method. However, the high operating temperature (≈100 K higher than the melting point of crystal) in Bridgman method could result in a slightly different stoichiometry due to the loss of volatile element and the contamination from the container. Therefore, single crystals of GeSe were synthesized through the chemical vapor transport method^[38] at the temperature range as low as possible. High-purity stoichiometric total

amount (≈ 1 g) of Ge and Se powder, together with 1.5 mg cm^{-3} iodine as the transport, were sealed in a quartz tube of 1.4 cm inner diameter and ≈ 15 cm length. To avoid the impurity formation, the raw materials were purified by sublimation and polishing before use. The vapor transport reaction was carried out in a two-zone furnace between 783 K (source) and 683 K (sink) for 10 days. The as-grown single crystals exhibit planar bar shape with a typical size of ≈ 2 to ≈ 5 mm. The phase purity was checked by powder x-ray diffraction of crushed single crystals. The single crystal quality and crystallization directions and were identified by Laue diffraction (Photonic Science).

TGA/DSC: Thermogravimetry analysis (TGA) and differential scanning calorimetry (DSC) (Figure S13, Supporting Information) were performed on a NETZSCH STA 449 F3 system under flowing air. The samples were gradually heated from 30 to 300 °C at a constant rate of 10 °C min^{-1} .

Computational Methods: The atomic structure and energetics of adsorption and oxidation were studied by density functional theory approaches implemented in the QUANTUM-ESPRESSO pseudopotential code [39] with taking into account the GGA-PBE + vdW approximation.[40] This computational framework is feasible for the description of the adsorption and decomposition of molecules on surfaces.[23] The energy cutoffs were 25 and 400 Ry for the plane-wave expansion of the wave functions and the charge density, respectively. The $3 \times 6 \times 6$ Monkhorst-Pack k -point grid for the Brillouin sampling was used for all considered systems.[41] For the modelling of the GeSe surface, the authors used a slab of four layers of $1 \times 2 \times 2$ supercell of GeSe.

The separation between layers within periodic boundary conditions was more than 25 \AA , thus excluding contribution from the interactions between the slabs.

For the bulk surface, optimization of only the atomic positions was carried out. For modelling the monolayer, we additionally allowed the optimization of lattice parameters.

The enthalpies of physisorption were calculated by:

$$\Delta H_{\text{phys}} = [E_{\text{host+mol}} - (E_{\text{host}} + E_{\text{guest}})] \quad (1)$$

where E_{host} is the total energy of pristine surface and E_{guest} is the energy of the single molecules of selected species in empty box. Note that for all adsorbates, we only considered the gaseous phase at low concentration, thus molecule–molecules interaction in gaseous phase did not include in E_{guest} . The chemisorption energy is defined as the difference between the total energy of the system with adsorbed molecule and the total energy of same system after decomposition of the same molecule on the surface. For the case of physisorption, we also estimated differential Gibbs free energy by further formula:

$$\Delta G = \Delta H - T\Delta S \quad (2)$$

where T is the temperature and ΔS is the change of entropy of adsorbed molecule, which was estimated considering the gas→liquid transition by the standard formula:

$$\Delta S = \Delta H_{\text{vaporization}} / T \quad (3)$$

where $\Delta H_{\text{vaporization}}$ is empirical enthalpy of vaporization.

For modelling the surface of the bulk crystal, the authors performed calculations with the optimization of the only atomic positions. Lattice parameters in these calculations were rigid and the same of the bulk crystal. For modelling monolayers, we instead optimized both atomic positions and lattice parameters. Thus, their model considers contributions from additional degrees of freedom of free-standing membranes. It is worth mentioning that the contributions related to the expansion or contraction of monolayer were essential for a correct evaluation of the chemical stability of metal monochalcogenides, as we demonstrated previously for the cases of InSe and GaSe nanosheets.[23]

X-Ray Photoemission Spectroscopy: Photoelectron spectroscopy measurements were performed at room temperature, in two different experimental apparatuses, both equipped with Scienta R3000 hemispherical electron analyzers. NAP-XPS measurements were

performed using Al K_{α} at the Charles University in Prague, while soft-x ray synchrotron radiation XPS was performed in UHV conditions (base pressure $< 10^{-10}$ mbar) at the CNR beamline BACH in Trieste, Italy. These two different XPS facilities were used in order to achieve complementary information. Synchrotron-based XPS enables high resolution, fast data acquisition and tunable photon energy, while NAP-XPS allows the measurements directly in a high-pressure chamber (1 mbar O_2 and H_2O vapor), where the sample was kept in conditions close to the ambient environment during data acquisition.

The NAP-XPS setup requires a special differentially pumped analyzer connected to the chamber hosting the sample. The entrance of the electron analyzer-lens system was equipped with a small pressure reducing orifice between the sample environment and the first pumping stage of the spectrometer. In the authors' case, the orifice was part of a specially designed NAP cell, which had to be docked to the analyzer when high pressure measurements were performed. Dosage of water vapor and oxygen (purity $\geq 99.9999\%$ vol.) was performed by precision leak valves, which were mounted in the NAP cell manipulator. In particular, H_2O vapor was obtained from liquid water (milliQ) purified with freeze pump thaw cycles until no traces of contaminations were detected by residual gas analyzer. The implantation of defects was performed by sputtering with Ar ions ($p = 10^{-5}$ mbar), with energy from 1.0 to 2.5 keV. A Shirley backgrounds was subtracted from raw XPS spectra and the resulting peaks were fitted with by a superposition of Voigt doublets.

X-Ray Photoemission Electron Microscopy: XPEEM measurements were carried out using a spectroscopic photoemission and low-energy electron microscope (SPELEEM) located at the Nanospectroscopy beamline (Elettra, Trieste).[42] In this instrument, the chemical information provided by XPEEM [43] was combined with the structural information given by low-energy electron microscopy (LEEM).[44] The spatial resolution in XPEEM mode was ≈ 30 nm, and the energy resolution was 0.3 eV in imaging spectroscopy. Moreover, imaging the back-focal plane of the instrument allowed us to acquire low energy electron diffraction patterns from micron-sized regions.

Liquid-Phase Exfoliation of GeSe: We performed sonication-assisted liquid-phase exfoliation to get nanosheets imaged in XPEEM spectra in Figures 5 and 6. First, GeSe crystals were finely grinded using a mortar. Afterward, 20 mg of powdered GeSe were added to 40 mL of isopropyl alcohol (IPA, ACS Reagent, $\geq 99.8\%$, Sigma-Aldrich), and ultrasonicated via tip sonication with a Sonics VC 505 instrument (Sonics, 20 kHz frequency and 500 W maximum power) at power output of 90% for 180 min in a thermostat bath ($T \leq 25 \text{ °C}$) to prevent excessive temperature rise. After a first high-speed centrifugation, at which supernatant was discarded and substituted with analogous amount of fresh IPA, a last centrifugation at 1000 rpm was performed to collect thinner flakes for characterization. For liquid-phase exfoliation with ethanol (Figure S10a, Supporting Information), *N*-methyl-2-pyrrolidone (NMP) (Figure S10b, Supporting Information), and dimethyl 2-methylglutarate (Figure 7b) solvents, the same procedure used for IPA was adopted.

Field emission scanning electron microscope (FESEM) experiments on GeSe nanosheets in Figure 7 and Figure S10, Supporting Information, were carried out at the Microscopy Centre of University of L'Aquila with Gemini SEM 500, at an accelerating voltage of 2 kV.

Electrical Tests: 10 μL of dispersion of fresh-exfoliated GeSe in a concentration of 0.3 mg mL^{-1} were deposited on Si_3N_4 substrates provided with front side Pt finger type electrodes (30 micron apart) and back side heater, had been in situ annealed while “in operando” monitoring the base line electrical resistance (BLR). A typical operando BLR assessment cycle, as shown in Figure S11, Supporting Information, comprises a 25 °C stepwise increase/decrease of the operating temperature (OT) in the interval 25 °C–100 °C–25 °C, while recording the resistance in flowing dry air for a number of subsequent 5 identical cycles.

Supporting Information

Supporting Information is available from the Wiley Online Library or from the author.

Acknowledgements

A.P. thanks CERIC-ERIC for the access to the NAP-XPS facility and Elettra Sincrotrone Trieste for providing access to its synchrotron radiation facilities. S.N. and F.B. acknowledge funding from EUROFEL project (RoadMap Esfri), J.D.S., V.P., and A.P. thank Maria Giammatteo for technical support in SEM experiments at Microscopy Centre of University of L'Aquila.

Open access funding provided by Universita degli Studi dell'Aquila within the CRUI-CARE Agreement.

Conflict of Interest

The authors declare no conflict of interest.

Author Contributions

D.W.B., F.B., and S.N. contributed equally to this work. The project was conceived and coordinated by A.P. Theoretical model was elaborated by D.W.B. Surface-science experiments were performed by S.N. and F.B. (synchrotron-based XPS in Figure 4); L.P. and M.V. (NAP-XPS in Figure 5); T.O.M., M.P., F.G., and A.L. (μ -XPS, LEEM and XPEEM in Figures 6 and 7). XPS analysis was performed by S.N. and F.B. while PEEM analysis was performed by T.O.M., respectively. Samples were grown by C.N.K., C.S.L., and A.P. Liquid-phase exfoliation was carried out by J.D.S. and V.P. The paper was written by D.W.B., S.N., F.B., and A.P.

Data Availability Statement

The data that support the findings of this study are available from the corresponding author upon reasonable request.

Keywords

2D materials, density functional theory calculations, catalysis, germanium selenide, surface science

Received: June 28, 2021

Revised: August 4, 2021

Published online: September 17, 2021

- [1] a) K. S. Novoselov, *Rev. Mod. Phys.* **2011**, *83*, 837; b) A. K. Geim, *Rev. Mod. Phys.* **2011**, *83*, 851.
- [2] a) H. Döscher, T. Schmaltz, C. Neef, A. Thielmann, T. Reiss, *2D Mater.* **2021**, *8*, 022005; b) H. Huang, H. Shi, P. Das, J. Qin, Y. Li, X. Wang, F. Su, P. Wen, S. Li, P. Lu, *Adv. Funct. Mater.* **2020**, *30*, 1909035; c) C. H. A. Tsang, H. Huang, J. Xuan, H. Wang, D. Leung, *Renewable Sustainable Energy Rev.* **2020**, *120*, 109656; d) A. Di Gaspare, E. A. A. Pogna, L. Salemi, O. Balci, A. R. Cadore, S. M. Shinde, L. Li, C. di Franco, A. G. Davies, E. H. Linfield, A. C. Ferrari, G. Scamarcio, M. S. Vitiello, *Adv. Funct. Mater.* **2021**, *31*, 2008039.
- [3] K. Novoselov, *Nat. Mater.* **2007**, *6*, 720.
- [4] a) S. Suzuki, T. Iwasaki, K. K. H. De Silva, S. Suehara, K. Watanabe, T. Taniguchi, S. Moriyama, M. Yoshimura, T. Aizawa, T. Nakayama, *Adv. Funct. Mater.* **2021**, *31*, 2007038; b) C. Liu, X. Zou, M. C. Wu, Y. Wang, Y. Lv, X. Duan, S. Zhang, X. Liu, W. W. Wu, W. Hu, Z. Fan, L. Liao, *Adv. Funct. Mater.* **2021**, *31*, 2100781; c) L. Huang, T. Yang, L. W. Wong, F. Zheng, X. Chen, K. H. Lai, H. Liu, Q. H. Thi, D. Shen, C. S. Lee, Q. Deng, J. Zhao, T. H. Ly, *Adv. Funct. Mater.* **2021**, *31*, 2009166; d) W. Choi, S. Hong, Y. Jeong, Y. Cho, H. G. Shin, J. H. Park, Y. Yi, S. Im, *Adv. Funct. Mater.* **2021**, *31*, 2009436; e) D. Buckley, Z. R. Kudrynskiy, N. Balakrishnan, T. Vincent, D. Mazumder, E. Castanon, Z. D. Kovalyuk, O. Kolosov, O. Kazakova, A. Tzalenchuk, A. Patanè, *Adv. Funct. Mater.* **2021**, *31*, 2008967; f) H. Bouzid, R. Sahoo, S. J. Yun, K. Singh, Y. Jin, J. Jiang, D. Yoon, H. Y. Song, G. Kim, W. Choi, Y. M. Kim, Y. H. Lee, *Adv. Funct. Mater.* **2021**, *31*, 2102560.
- [5] a) J. Du, Q. Liao, B. Liu, X. Zhang, H. Yu, Y. Ou, J. Xiao, Z. Kang, H. Si, Z. Zhang, Y. Zhang, *Adv. Funct. Mater.* **2021**, *31*, 2007559; b) S. Roy, Z. Hu, S. Kais, P. Bermel, *Adv. Funct. Mater.* **2021**, *31*, 2100387.
- [6] L. Wang, D. Xu, L. Jiang, J. Gao, Z. Tang, Y. Xu, X. Chen, H. Zhang, *Adv. Funct. Mater.* **2021**, *31*, 2004408.
- [7] a) H. Jang, Y. Seok, Y. Choi, S. H. Cho, K. Watanabe, T. Taniguchi, K. Lee, *Adv. Funct. Mater.* **2021**, *31*, 2006788; b) P. Luo, F. Wang, J. Qu, K. Liu, X. Hu, K. Liu, T. Zhai, *Adv. Funct. Mater.* **2021**, *31*, 2008351.
- [8] W. Gao, Y. Zhou, X. Wu, Q. Shen, J. Ye, Z. Zou, *Adv. Funct. Mater.* **2021**, *31*, 2005197.
- [9] D. M. Kennes, L. Xian, M. Claassen, A. Rubio, *Nat. Commun.* **2020**, *11*, 1124.
- [10] S.-C. Liu, C.-M. Dai, Y. Min, Y. Hou, A. H. Proppe, Y. Zhou, C. Chen, S. Chen, J. Tang, D.-J. Xue, E. H. Sargent, J.-S. Hu, *Nat. Commun.* **2021**, *12*, 670.
- [11] Y. Ye, Q. Guo, X. Liu, C. Liu, J. Wang, Y. Liu, J. Qiu, *Chem. Mater.* **2017**, *29*, 8361.
- [12] G. Bianca, M. I. Zappia, S. Bellani, Z. k. Sofer, M. Serri, L. Najafi, R. Oropesa-Nuñez, B. Martín-García, T. s. Hartman, L. Leoncino, *ACS Appl. Mater. Interfaces* **2020**, *12*, 48598.
- [13] B. Zhang, X. Fu, L. Song, X. Wu, *J. Phys. Chem. Lett.* **2020**, *11*, 7664.
- [14] J. O. Island, G. A. Steele, H. S. J. van der Zant, A. Castellanos-Gomez, *2D Mater.* **2015**, *2*, 011002.
- [15] Y. Guo, S. Zhou, Y. Bai, J. Zhao, *ACS Appl. Mater. Interfaces* **2017**, *9*, 12013.
- [16] Y. Xu, K. Xu, C. Ma, Y. Chen, H. Zhang, Y. Liu, Y. Ji, *J. Mater. Chem. A* **2020**, *8*, 19612.
- [17] a) W. S. Yoo, J. H. Kim, S. M. Han, *J. Micro/Nanolithogr., MEMS, MOEMS* **2014**, *13*, 011205; b) P. Borowicz, *J. Spectrosc.* **2016**, *2016*, 1617063.
- [18] L. Shi, Q. Zhou, Y. Zhao, Y. Ouyang, C. Ling, Q. Li, J. Wang, *J. Phys. Chem. Lett.* **2017**, *8*, 4368.
- [19] D. Sarkar, S. Roychowdhury, R. Arora, T. Ghosh, A. Vasdev, B. Joseph, G. Sheet, U. V. Waghmare, K. Biswas, *Angew. Chem.* **2021**, *60*, 10350.
- [20] a) L. Shaabani, S. Aminorroaya-Yamini, J. Byrnes, A. Akbar Nezhad, G. R. Blake, *ACS Omega* **2017**, *2*, 9192; b) P. A. E. Murgatroyd, M. J. Smiles, C. N. Savory, T. P. Shalvey, J. E. N. Swallow, N. Fleck, C. M. Robertson, F. Jäckel, J. Alaria, J. D. Major, D. O. Scanlon, T. D. Veal, *Chem. Mater.* **2020**, *32*, 3245.
- [21] C. Wang, K. Wang, D. Huang, L. Li, K. Feng, N. A. Abdel Ghany, L. Zhao, F. Jiang, *CrystEngComm* **2021**, *23*, 762.
- [22] a) H. Ren, M. P. Humbert, C. A. Menning, J. G. Chen, Y. Shu, U. G. Singh, W. C. Cheng, *Appl. Catal., A* **2010**, *375*, 303; b) D. J. D. Durbin, C. Malardier-Jugroot, *J. Phys. Chem. C* **2010**, *115*, 808; c) C. Farrell, C. Gardner, M. Ternan, *J. Power Sources* **2007**, *171*, 282; d) Q. Li, R. He, J.-A. Gao, J. O. Jensen, N. J. Bjerrum, *J. Electrochem. Soc.* **2003**, *150*, A1599.
- [23] G. D'Olimpio, S. Nappini, M. Vorokhta, L. Lozzi, F. Genuzio, T. O. Menteg, V. Paolucci, B. Gürbulak, S. Duman, L. Ottaviano, A. Locatelli, F. Bondino, D. W. Boukhalov, A. Politano, *Adv. Funct. Mater.* **2020**, *30*, 2005466.

- [24] Q. Wu, W. Wei, X. Lv, B. Huang, Y. Dai, *J. Phys. Chem. C* **2019**, *123*, 11791.
- [25] Y. Ji, M. Yang, H. Dong, T. Hou, L. Wang, Y. Li, *Nanoscale* **2017**, *9*, 8608.
- [26] a) S. Z. Rahaman, S. Maikap, A. Das, A. Prakash, Y. H. Wu, C.-S. Lai, T.-C. Tien, W.-S. Chen, H.-Y. Lee, F. T. Chen, M.-J. Tsai, L.-B. Chang, *Nanoscale Res. Lett.* **2012**, *7*, 614; b) X. Li, X. Zhang, X. Lv, J. Pang, L. Lei, Y. Liu, Y. Peng, G. Xiang, *Nanotechnology* **2020**, *31*, 285702.
- [27] S. Rahaman, S. Maikap, W. Chen, H. Lee, F. Chen, T. Tien, M. Tsai, *J. Appl. Phys.* **2012**, *111*, 063710.
- [28] a) D. Wang, G. He, Z. Fang, L. Hao, Z. Sun, Y. Liu, *RSC Adv.* **2020**, *10*, 938; b) V. Grossi, P. Parisse, M. Passacantando, S. Santucci, G. Impellizzeri, A. Irrera, L. Ottaviano, *Appl. Surf. Sci.* **2008**, *254*, 8093.
- [29] a) M. A. Ruiz-Fresneda, A. S. Eswayah, M. Romero-González, P. H. E. Gardiner, P. L. Solari, M. L. Merroun, *Environ. Sci.: Nano* **2020**, *7*, 2140; b) M. Shenasa, S. Sainkar, D. Lichtman, *J. Electron Spectrosc. Relat. Phenom.* **1986**, *40*, 329.
- [30] A. Mura, I. Hideshima, Z. Liu, T. Hosoi, H. Watanabe, K. Arima, *J. Phys. Chem. C* **2013**, *117*, 165.
- [31] A. Azcatl, S. Kc, X. Peng, N. Lu, S. McDonnell, X. Qin, F. de Dios, R. Addou, J. Kim, M. J. Kim, K. Cho, R. M. Wallace, *2D Mater.* **2015**, *2*, 014004.
- [32] a) J. Pola, R. Fajgar, Z. Bastl, L. Diaz, *J. Mater. Chem.* **1992**, *2*, 961; b) K. Prabhakaran, T. Ogino, *Surf. Sci.* **1995**, *325*, 263.
- [33] S. Tanuma, C. J. Powell, D. R. Penn, *Surf. Interface Anal.* **2011**, *43*, 689.
- [34] X. Zhou, P. Gao, S. Sun, D. Bao, Y. Wang, X. Li, T. Wu, Y. Chen, P. Yang, *Chem. Mater.* **2015**, *27*, 6730.
- [35] a) L. Xu, Q. Wu, H. Chang, G. Li, J. Zou, S. Wang, *Fuel* **2020**, *269*, 117435; b) E. Xu, P. Li, J. Quan, H. Zhu, L. Wang, Y. Chang, Z. Sun, L. Chen, D. Yu, Y. Jiang, *Nano-Micro Lett.* **2021**, *13*, 40.
- [36] a) S. Wageh, M. Maize, S. Han, A. A. Al-Ghamdi, X. Fang, *RSC Adv.* **2014**, *4*, 24110; b) M. A. Farrukh, I. Muneer, K. M. Butt, S. Batool, N. Fakhar, *J. Chin. Chem. Soc.* **2016**, *63*, 952.
- [37] N. T. K. Thanh, N. Maclean, S. Mahiddine, *Chem. Rev.* **2014**, *114*, 7610.
- [38] a) H. I. Wiedemeier, E. A. Irene, A. K. Chaudhuri, *J. Cryst. Growth* **1972**, *13-14*, 393; b) H. Wiedemeier, E. A. Irene, *Z. Anorg. Allg. Chem.* **1973**, *400*, 59.
- [39] P. Giannozzi, S. Baroni, N. Bonini, M. Calandra, R. Car, C. Cavazzoni, D. Ceresoli, G. L. Chiarotti, M. Cococcioni, I. Dabo, A. Dal Corso, S. de Gironcoli, S. Fabris, G. Fratesi, R. Gebauer, U. Gerstmann, C. Gougoussis, A. Kokalj, L. Michele, L. Martin-Samos, N. Marzari, F. Mauri, R. Mazzarello, S. Paolini, A. Pasquarello, L. Paulatto, C. Sbraccia, S. Scandolo, G. Sclauzero, A. P. Seitsonen, et al., *J. Phys.: Condens. Matter* **2009**, *21*, 395502.
- [40] a) J. P. Perdew, K. Burke, M. Ernzerhof, *Phys. Rev. Lett.* **1996**, *77*, 3865; b) V. Barone, M. Casarin, D. Forrer, M. Pavone, M. Sambri, A. Vittadini, *J. Comput. Chem.* **2009**, *30*, 934.
- [41] H. J. Monkhorst, J. D. Pack, *Phys. Rev. B* **1976**, *13*, 5188.
- [42] a) A. Locatelli, L. Aballe, T. O. Montes, M. Kiskinova, E. Bauer, *Surf. Interface Anal.* **2006**, *38*, 1554; b) T. Montes, G. Zamborlini, A. Sala, A. Locatelli, *Beilstein J. Nanotechnol.* **2014**, *5*, 1873.
- [43] A. Locatelli, E. Bauer, *J. Phys.: Condens. Matter* **2008**, *20*, 093002.
- [44] E. Bauer, *Surface Microscopy with Low Energy Electrons*, Springer, Berlin, Germany **2014**.